Nuclear Science and Techniques (2025) 36:169
https://doi.org/10.1007/s41365-025-01753-w

α decay and cluster radioactivity in extreme laser fields

Hui Wang[1] · Ying-Ge Huang[1] · Ze-Peng Gao[1] · Jia-Li Huang[1] · Er-Xi Xiao[1] · Long Zhu[1] · Jun Su[1]

Received: 5 November 2024 / Revised: 8 December 2024 / Accepted: 2 February 2025 / Published online: 29 June 2025

Abstract
The potential of high-intensity lasers to influence nuclear decay processes has attracted considerable interest. This study quantitatively evaluated the effects of high-intensity lasers on α decay and cluster radioactivity. Our calculations revealed that, among the parent nuclei investigated, ^{144}Nd is the most susceptible to laser-induced alterations, primarily because of its relatively low decay energy. Additionally, circularly polarized lasers exhibit a greater impact on decay modifications than linearly polarized lasers. Given the limited time resolution of current detectors, it is essential to account for the time-averaging effect of the laser. By incorporating the effects of circular polarization, time averaging, and angular averaging, our theoretical predictions indicated that the modification of ^{144}Nd decay could reach 0.1% at an intensity of 10^{27} W/cm^2. However, this intensity significantly exceeds the current laser capability of 10^{23} W/cm^2, and the predicted modification of 0.1% remains below the detection threshold of contemporary measurement techniques. Observing laser-assisted α decay and ^{14}C cluster radioactivity will likely remain unfeasible until both ultrahigh laser intensities and significant advancements in experimental resolution are achieved.

Keywords Extreme laser field · Frozen Hartree–Fock method · α decay · Cluster radioactivity

1 Introduction

The field of research concerning the interactions of strong laser fields with atoms and molecules has reached a considerable degree of maturity [1–3]. Recently, projects for extremely high-intensity lasers have been proposed by the Shanghai Ultra Intensive Ultrafast Laser Facility [4, 5], the Extreme Light Infrastructure for Nuclear Physics [6, 7], and a Russian group [8]. Because of the enhancements envisaged for the near future, laser-driven nuclear physics has attracted increasing interest and extensive research has been performed on, for example, the impact of laser fields on α decay [9–19], proton emission [6, 12, 20], cluster radioactivity [12, 18], nuclear fission [12], nuclear fusion [21–23], and nuclear excitation [24–26]. Among these, significant attention has been paid to the α decay of nuclei under the influence of strong laser fields.

α decay is crucial in nuclear physics because it provides information on the nuclear structure [27–29] and facilitates the understanding of topics such as the nuclear transformation between the liquid state and cluster state [30, 31]. α radioactivity was first discovered by Rutherford in 1903. Following this discovery, many attempts were made to modify α decay rates by changing the temperature, pressure, and magnetic and gravitational fields [32, 33]. The changes in the decay constant were small and could be neglected. These interpretations may stem from Gamow's explanation of quantum-mechanical tunneling [34], according to which α decay is correlated with the width through the potential. The distortions in the potential and changes in the decay energy modified by the above experiments were negligible, and no effect was detected. The remarkable developments in laser technology provide an alternative method to explore and advance this study.

Lasers interact with matter through two fundamental mechanisms: single-photon and electromagnetic field interactions. The former is not feasible for nuclear processes because of the significant energy discrepancy between a single photon (on the order of 1 eV) and nuclear energy levels (on the order

This work was supported by the National Natural Science Foundation of China (Nos. 12475136 and 12075327).

✉ Jun Su
sujun3@mail.sysu.edu.cn

[1] Sino-French Institute of Nuclear Engineering and Technology, Sun Yat-sen University, Zhuhai 519082, China

of 1 MeV). When the laser intensity is sufficiently high, the laser–matter interaction is predominantly governed by the electromagnetic field [3], which is believed to possess the potential to control nuclear systems. Thus, many studies have focused on the necessity of high-intensity lasers to modify decay processes [9–19]. According to Ref. [11], no significant modification of α decay is expected with the lasers currently available or those anticipated for the forthcoming years.

However, some recent studies have indicated the substantial effect of current laser intensities on α decay by solving the time-dependent Schrödinger equation within the oscillating Kramers–Henneberger frame [15–19]. Others suggest a small yet detectable influence at the current laser intensities or those that will be attained in the foreseeable future [9, 10, 12–14]. The inconsistencies in these findings highlight the ongoing debate and the lack of a clear consensus. Moreover, the temporal and angular effects and variation in the spatial shape of the laser field are intriguing for experiments; however, these remain ambiguous. In this study, we investigated the influence of extreme laser fields on nuclear α decay using the frozen Hartree–Fock (FHF) approach [35–37]. In contrast to the aforementioned approaches, it can compute the microscopic internuclear potential and deformation effects in a self-consistent manner [38–40]. Cluster radioactivity has been investigated since 1984 [41] as an intermediate process between α decay and spontaneous fission [42–44], and it has deepened our understanding of decay mechanics. Thus, it would also be interesting to study cluster radioactivity.

The remainder of this paper is organized as follows. Section 2 introduces the theoretical framework for laser-assisted particle decay using the FHF method. Section 3 presents and discusses the results. Finally, Sect. 4 presents the conclusions of this study.

2 Theoretical framework

2.1 Unified formula of half-lives for α decay and cluster radioactivity

α-decay and cluster radioactivity processes can be interpreted within a unified tunneling framework following Gamow's depiction [44–46]. The emitted particles are assumed to preform on the surface of the parent nucleus with varying preformation probabilities [47, 48] and eventually penetrate the potential barrier by constantly hitting it. The unified formula for the half-lives of α decay and cluster radioactivity is expressed as follows:

$$T_{1/2} = \frac{\hbar \ln 2}{FPS_{\rm pre}}, \tag{1}$$

where $\hbar$ is the reduced Planck constant, F is the impinging frequency that hits the barrier, P is the possibility of penetration, and $S_{\rm pre}$ is the preformation factor.

The impinging frequency F is expressed as follows:

$$F = \frac{\sqrt{2E_{\rm k}/\mu}}{R_{\rm in}}, \tag{2}$$

where $R_{\rm in}$ is the tunneling entrance point, and $E_{\rm k}$ is the kinetic energy of the emitted particle, which can be expressed as $E_{\rm k} = \frac{A_{\rm d}}{A_{\rm e}+A_{\rm d}} Q_{\rm e}$. The reduced mass of the emitted particle and daughter nucleus μ can be written as

$$\mu = \frac{A_{\rm e}A_{\rm d}}{A_{\rm e}+A_{\rm d}}, \tag{3}$$

where $A_{\rm e}$ and $A_{\rm d}$ are the masses of the emitted particle and daughter nucleus, respectively.

The penetration possibility P is determined using the Wentzel–Kramers–Brillouin (WKB) approximation. Considering the nuclear deformation effect, the total penetration possibility $P(t,\theta,I)$ is obtained by integrating $P(t,\phi,\theta,I)$ in all directions,

$$\begin{aligned} P(t,\theta,I) &= \frac{1}{2}\int_0^{\pi} P(t,\phi,\theta,I)\sin\phi \mathrm{d}\phi, \\ P(t,\phi,\theta,I) &= \exp\left[-\frac{2(2\mu)^{1/2}}{\hbar}\int_{R_{\rm in}}^{R_{\rm out}} k(r,t,\phi,\theta,I)\mathrm{d}r\right], \\ k(r,t,\phi,\theta,I) &= \sqrt{|V(r,t,\phi,\theta,I)-Q_{\rm e}|}, \end{aligned} \tag{4}$$

where ϕ denotes the angle between the principal axis of the daughter nucleus and the particle emission direction. θ represents the angle between the directions of the laser field and particle emission. I denotes the laser intensity. $R_{\rm in}$ and $R_{\rm out}$ are the tunneling entrance and exit points, respectively. These points are determined by the condition $V(r,t,\phi,\theta,I) = Q_{\rm e}$, where $Q_{\rm e}$ is the decay energy of the emitted particle. $V(r,t,\phi,\theta,I)$ is the total potential with the intervention of the laser field, which is expressed as

$$V(r,t,\phi,\theta) = V_{\rm N}(r,\phi) + V_{\rm c}(r,\phi) + V_l(r) + V_{\rm i}(r,t,\phi,\theta,I), \tag{5}$$

where $V_{\rm N}$ and $V_{\rm c}$ denote the nuclear and Coulomb potentials, respectively. Both are calculated using the FHF method. The centrifugal potential V_l is given by

$$V_l(r) = \frac{l(l+1)\hbar^2}{2\mu r^2}, \tag{6}$$

where l is the corresponding angular momentum quantum number of the emitted particle. The decay channel, decay energy, angular momentum, and experimental half-life are listed in Table 1. $V_{\rm i}$ represents the interaction between the

laser field and the decay system, which is described in detail in the following subsection.

The uniform values or formulas for the preformation factor $S_{\rm pre}$ in Eq. (1) have been established [49–52]. For α decay, we adopt the following values [51]:

$$\begin{aligned} S_{\rm pre} &= 0.38 \text{ (even-even nuclei)},\\ S_{\rm pre} &= 0.24 \text{ (odd-even nuclei)},\\ S_{\rm pre} &= 0.13 \text{ (odd-odd nuclei)}. \end{aligned} \tag{7}$$

Cluster radioactivity [53] is adopted as

$$\begin{aligned} S_{\rm pre} &= 10^{-0.01674 Z_{\rm e} Z_{\rm d} + 2.035466} \text{(even-even nuclei)},\\ S_{\rm pre} &= 10^{-0.01674 Z_{\rm e} Z_{\rm d} + 2.035466 - 1.175} \text{(odd-}A\text{ nuclei)}, \end{aligned} \tag{8}$$

where $Z_{\rm e}$ and $Z_{\rm d}$ are the number of protons in the emitted particle and daughter nucleus, respectively.

2.2 The frozen Hartree–Fock method

The nucleus–nucleus interaction potential, which consists of the nuclear potential $V_{\rm N}$ and Coulomb potential $V_{\rm c}$, is utilized to substitute the corresponding terms in Eq. (5). This potential was calculated using the FHF method, which requires frozen ground-state densities ρ_i of the two nuclei at all distances. The resulting nucleus–nucleus interaction potential, referred to as the FHF potential in this context, is expressed as follows:

$$V_{\rm FHF}(\boldsymbol{R}) = \int H[\rho_1(\boldsymbol{r}) + \rho_2(\boldsymbol{r}-\boldsymbol{R})]{\rm d}\boldsymbol{r} - E[\rho_1] - E[\rho_2]. \tag{9}$$

The first term on the right-hand side of Eq. (9) represents the total energy of the system when a distance vector $\boldsymbol{R}$ is placed between the centers of mass of the two nuclei. $E[\rho_i]$ is the binding energy of each nucleus ($i = 1, 2$). To compute the FHF potential, one must first determine the Hartree–Fock ground states of the two nuclei separately. Energy $E[\rho_i]$ is inherently obtained in the static Hartree–Fock process. The first term on the right side of Eq. (9) is calculated by placing the two aforementioned static Hartree–Fock solutions at a distance $\boldsymbol{R}$ from each other in a TDHF code [54–56] without a boost and computing the energy of the combined system, including the Coulomb contribution [57]. The above calculations are performed in three-dimensional Cartesian geometry without symmetry assumptions and utilizing the Skyrme energy density functional Sly5 [58]. The box sizes for the Hartree–Fock calculations were selected to be 28^3 fm^3 and 28 fm × 28 fm × 100 fm. The mesh spacing is 1.0 fm in all directions.

2.3 Laser–nucleus interaction

In this context, a laser field, known as an electromagnetic field, is treated as an electric field. In fact, the magnetic part can be neglected because the subbarrier motion of the emitted particles under investigation remains nonrelativistic. Generally, the wavelength of the laser fields (near-ultraviolet to near-infrared) is much larger than the nuclear length scale (on the order of a femtometer). The dipole approximation can thus be used for the laser electric field, which is given in the length gauge as

$$V_{\rm i}(r, t, \phi, \theta, I) = -Q_{\rm eff}\boldsymbol{r}\boldsymbol{E}(t), \tag{10}$$

where

$$Q_{\rm eff} = \frac{Z_{\rm e}A_{\rm d} - Z_{\rm d}A_{\rm e}}{A_{\rm e} + A_{\rm d}}, \tag{11}$$

is the effective charge, which represents the tendency of the laser electric field to separate the two nuclei in the decay system. $Z_{\rm e}$ and $Z_{\rm d}$ are the proton numbers of the emitted particle and the daughter nucleus, respectively. The laser electric field also influences the decay energy. Similarly, the change in the decay energy $\Delta Q_{\rm e}$ is expressed as

$$\Delta Q_{\rm e} = eZ_{\rm e}\boldsymbol{R}_{\rm d}(\phi)\boldsymbol{E}(t), \tag{12}$$

where $\boldsymbol{R}_{\rm d}$ is the radius of the daughter nucleus that the emitted particle penetrates. The decay energy induced by the laser field is given by

$$Q_{\rm e}^{*} = Q_{\rm e} + \Delta Q_{\rm e}. \tag{13}$$

In addition, the time required for the emitted particles to penetrate the potential barrier can be estimated. Considering α particles traveling through a barrier of width $l \simeq 50$ fm with decay energy of 10 MeV, the traversal time was calculated as approximately 10^{-21} s. One optical cycle for the 800-nm laser field is on the order of femtoseconds. Consequently, the laser electric field can be treated in the quasi-static approximation, that is, the laser field is viewed as static during particle penetration through the barrier.

The effect of the spatial shape of the laser on the decay processes is of interest. In this study, we consider two types of laser shapes, which are expressed as follows:

$$\begin{aligned} \boldsymbol{E}(t) &= E_0 \sin\left(\frac{2\pi ct}{\lambda}\right)\boldsymbol{e}_r \text{ (linear polarization)},\\ \boldsymbol{E}(t) &= E_0\left(\sin\left(\frac{2\pi ct}{\lambda}\right)\boldsymbol{e}_x + \cos\left(\frac{2\pi ct}{\lambda}\right)\boldsymbol{e}_y\right)\\ &\quad \text{(circular polarization)}, \end{aligned} \tag{14}$$

where c is the speed of light, and λ is the laser wavelength (800 nm is used here). The peak electric field strength E_0 can be represented by the laser intensity I, which is given by:

$$E_0 = 27.44\sqrt{I}. \tag{15}$$

Here, the units of E_0 and I are V/cm and W/cm^2, respectively.

2.4 Relative change of penetration possibility ΔP

The FHF method ignores the dynamic effects and Pauli repulsion between nucleons belonging to different nuclei [40, 57]. The latter is regarded as a significant factor in the preformation of the emitted particles on the surface of the parent nucleus. Moreover, our model is incapable of calculating the preformation factor, which remains a great challenge for the beyond-mean field theory. Therefore, this work focuses on the relative change in the penetration possibility induced by the laser field while ignoring the impact of the laser field on the preformation factor [11–14]. The relative change in the penetration possibility is defined as

$$\Delta P(t,\theta,I) = \frac{P(t,\theta,I) - P(t,\theta,I=0)}{P(t,\theta,I=0)}. \tag{16}$$

It should be noted that ΔP is a function of time t, emission angle θ, and intensity I. It is interesting to consider the temporal and angular effects of the laser field. The time-integrated modification of the penetration possibility can be expressed as follows:

$$\overline{\Delta P}_t(\theta,I) = \frac{1}{T}\int_0^T \Delta P(t,\theta,I)\mathrm{d}t. \tag{17}$$

The time- and angle-integrated modification is expressed as

$$\overline{\Delta P}_{t\theta}(I) = \frac{1}{2}\int_0^\pi \mathrm{d}\theta\overline{\Delta P}_t(\theta,I)\sin\theta. \tag{18}$$

To elucidate the laser modification of the penetration possibility, it is necessary to further investigate the formula for ΔP. We begin with the penetration possibility, $P(t,\phi,\theta,I)$.

$$\begin{aligned} P(t,\phi,\theta,I) &= \exp\left[-\frac{2(2\mu)^{1/2}}{\hbar}\int_{R_{\mathrm{in}}}^{R_{\mathrm{out}}} \times\sqrt{V(r,t,\phi,\theta,I) - Q_{\mathrm{e}}^*}\mathrm{d}r\right] \\ &= \exp\left[-\frac{2(2\mu)^{1/2}}{\hbar}\int_{R_{\mathrm{in}}}^{R_{\mathrm{out}}}\sqrt{V_0(r)} \times\sqrt{1+\frac{V_{\mathrm{i}}(r,t,\phi,\theta,I)-\Delta Q_{\mathrm{e}}}{V_0(r)}}\mathrm{d}r\right], \end{aligned} \tag{19}$$

where $V_0(r) = V_{\mathrm{FHF}}(r) + V_l(r) - Q_{\mathrm{e}}$. Assuming $|V_{\mathrm{i}} - \Delta Q_{\mathrm{e}}| \ll V_0$, we proceed with the Taylor expansion of Eq. (19).

$$\begin{aligned} P(t,\phi,\theta,I) &\approx \exp\left[\gamma^{(0)} + \gamma^{(1)} + \gamma^{(2)}\right] \\ &= \exp(\gamma^{(0)})\exp(\gamma^{(1)} + \gamma^{(2)}), \end{aligned} \tag{20}$$

where $\gamma^{(0)}$, $\gamma^{(1)}$ and $\gamma^{(2)}$ are given by

$$\begin{aligned} \gamma^{(0)} &= -\frac{2(2\mu)^{1/2}}{\hbar}\int_{R_{\mathrm{in}}}^{R_{\mathrm{out}}}\mathrm{d}r\sqrt{V_0(r)}, \\ \gamma^{(1)} &= -\frac{(2\mu)^{1/2}}{\hbar}\int_{R_{\mathrm{in}}}^{R_{\mathrm{out}}}\mathrm{d}r\frac{V_{\mathrm{i}}(r,t,\phi,\theta,I)-\Delta Q_{\mathrm{e}}}{\sqrt{V_0(r)}}, \\ \gamma^{(2)} &= \frac{(2\mu)^{1/2}}{\hbar}\int_{R_{\mathrm{in}}}^{R_{\mathrm{out}}}\mathrm{d}r\frac{(V_{\mathrm{i}}(r,t,\phi,\theta,I)-\Delta Q_{\mathrm{e}})^2}{4V_0^{3/2}(r)}. \end{aligned} \tag{21}$$

Note that $\exp(\gamma^{(0)})$ is approximately equal to the laser-free penetration possibility $P(t,\phi,\theta,I=0)$ and the relative change in the penetration possibility is given by

$$\begin{aligned} \Delta P(t,\phi,\theta,I) &\approx \frac{\exp(\gamma^{(0)})\exp(\gamma^{(1)}+\gamma^{(2)}) - \exp(\gamma^{(0)})}{\exp(\gamma^{(0)})} \\ &= \exp(\gamma^{(1)}+\gamma^{(2)}) - 1 \\ &\approx \gamma^{(1)} + \gamma^{(2)}. \end{aligned} \tag{22}$$

$\gamma^{(1)} + \gamma^{(2)}$ tends to zero because we assume that $|V_{\mathrm{i}} - \Delta Q_{\mathrm{e}}| \ll V_0$. Given the analysis of diverse spatial profiles of the laser in this study, it is necessary to provide detailed formulations for $\gamma^{(1)}$ and $\gamma^{(2)}$. For linear polarization, it follows that

$$\begin{aligned} \gamma^{(1)} &= \frac{27.44(2\mu)^{1/2}}{\hbar}\sqrt{I}\sin\left(\frac{2\pi ct}{\lambda}\right)\cos\theta \\ &\quad\times\int_{R_{\mathrm{in}}}^{R_{\mathrm{out}}}\mathrm{d}r\frac{Q_{\mathrm{eff}}r + eZ_{\mathrm{e}}R_{\mathrm{in}}(\phi)}{\sqrt{V_0(r)}}, \\ \gamma^{(2)} &= \frac{188.24(2\mu)^{1/2}}{\hbar}I\sin^2\left(\frac{2\pi ct}{\lambda}\right)\cos^2\theta \\ &\quad\times\int_{R_{\mathrm{in}}}^{R_{\mathrm{out}}}\mathrm{d}r\frac{(Q_{\mathrm{eff}}r + eZ_{\mathrm{e}}R_{\mathrm{in}}(\phi))^2}{V_0^{3/2}(r)}. \end{aligned} \tag{23}$$

For circular polarization, it follows that

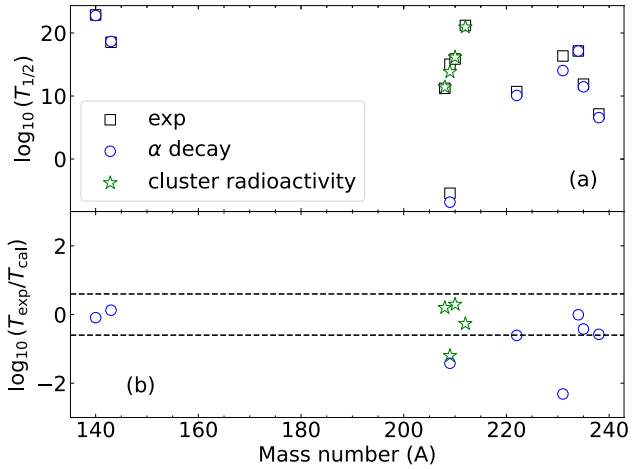

Fig. 1 (Color online) **a** Experimental and calculated half-lives for different parent nuclei. The black squares represent the experimental data. The blue circles represent the calculated α decay half-lives of the ground state parent nuclei ^{144}Nd, ^{226}Ra, ^{238}U, ^{242}Cm, ^{147}Sm, ^{213}Po, ^{235}U, and ^{239}Pu. The green stars represent the calculated ^{14}C cluster radioactivity half-lives of the ground state parent nuclei ^{222,223,224,226}Ra. **b** The corresponding logarithms of hindrance factors (HF = $T_{\rm exp}/T_{\rm cal}$)

$$\gamma^{(1)} = \frac{27.44(2\mu)^{1/2}}{\hbar}\sqrt{I}\left(\sin\left(\frac{2\pi ct}{\lambda}\right)\cos\theta + \cos\left(\frac{2\pi ct}{\lambda}\right)\sin\theta\right) \times \int_{R_{\rm in}}^{R_{\rm out}} {\rm d}r \frac{Q_{\rm eff}r + eZ_{\rm e}R_{\rm in}(\phi)}{\sqrt{V_0(r)}},$$
$$\gamma^{(2)} = \frac{188.24(2\mu)^{1/2}}{\hbar}I\left(\sin\left(\frac{2\pi ct}{\lambda}\right)\cos\theta + \cos\left(\frac{2\pi ct}{\lambda}\right)\sin\theta\right)^2 \times \int_{R_{\rm in}}^{R_{\rm out}} {\rm d}r \frac{(Q_{\rm eff}r + eZ_{\rm e}R_{\rm in}(\phi))^2}{V_0^{3/2}(r)}. \quad (24)$$

3 Results

Figure 1a shows a comparison of the experimental and theoretical half-lives. The corresponding deviations between the logarithms of the experimental half-lives and the calculated values are shown in Fig. 1b. The blue circles represent the calculated α decay of the ground-state parent nuclei ^{144}Nd, ^{226}Ra, ^{238}U, ^{242}Cm, ^{147}Sm, ^{213}Po, ^{235}U, and ^{239}Pu. The green stars represent the calculated ^{14}C cluster radioactivity of the ground-state parent nuclei, ^{222,223,224,226}Ra. It can be observed that the difference between the calculated values and experimental data is small. The values of $\log_{10}(T_{\rm exp}/T_{\rm cal})$ for α decay and cluster radioactivity were generally within the range of approximately ± 0.6. These values correspond to the values of the ratio $T_{\rm exp}/T_{\rm cal}$ within the range of approximately 0.25−3.98. This demonstrates the reliability of our model for predicting half-lives. Detailed information regarding the experimental and calculated data is presented in Table 1.

Table 1 Experimental and calculated half-lives (in seconds) of α decay and cluster radioactivity

Decay channels	Q_e (MeV)	l	$\log_{10}T_{\rm exp}$	$\log_{10}T_{\rm cal}$	$\log_{10}$HF
^{144}Nd →^{140} Ce+α	1.90	0	22.86	22.77	0.09
^{226}Ra →^{222} Rn+α	4.87	0	10.70	10.09	0.61
^{238}U →^{234} Th+α	4.27	0	17.15	17.14	0.01
^{242}Cm →^{238} Pu+α	6.23	0	7.15	6.57	0.58
^{147}Sm →^{143} Nd+α	2.31	0	18.53	18.66	−0.13
^{213}Po →^{209} Pb+α	8.54	0	−5.43	−6.85	1.42
^{235}U →^{231} Th+α	4.68	1	16.35	14.04	2.31
^{239}Pu →^{235} U+α	5.25	3	11.88	11.46	0.42
^{222}Ra →^{208} Pb+^{14}C	33.05	0	11.22	11.42	−0.20
^{223}Ra →^{209} Pb+^{14}C	31.83	4	15.04	13.84	1.20
^{224}Ra →^{210} Pb+^{14}C	30.53	0	15.87	16.16	0.29
^{226}Ra →^{212} Pb+^{14}C	28.20	0	21.20	20.93	0.27

Q_e and l are the decay energy and the angular momentum quantum number of the emitted particle, respectively

The hindrance factor (HF) is defined as the ratio between the experimental and calculated half-lives (HF = $T_{\rm exp}/T_{\rm cal}$)

One typically assumes a spherical shape for the nuclei to simplify the calculation of α decay half-lives. However, nuclear deformation has been reported to significantly affect these calculations [50, 51]. Figure 2 shows the FHF potential of α +^{222} Rn for selected orientations. Because the α particle is spherical, the differences in these potentials stem from the orientation of the daughter nucleus ^{222}Rn. This shows that as the orientation rotates from the tip to the side, the Coulomb barrier increases and the nuclear part of the potential becomes shallower. This phenomenon can be attributed to the larger overlap of the nuclear density distribution in the tip orientation, which leads to a more pronounced effect on the nuclear potential. This also shows that the tunneling points differ by approximately 1 fm with varying orientations, resulting in an order-of-magnitude change in the penetration probability and subsequent alterations in α decay half-lives. In addition, the laser–nucleus interaction depends on the angle between the directions of the laser field and particle emission. It is inferred that nuclear deformation is a critical factor that should be incorporated into laser-assisted α decay and cluster radioactivity calculations.

To illustrate the influence of the laser field on the penetration process, a comparison of the laser-free internuclear potentials for the α +^{222} Rn system with the two laser-assisted cases is shown in Fig. 3. For simplicity, only the tip-orientation case is presented. The laser field induces a downward shift in the Coulomb portion of the potential and an increase in the α-decay energy, whereas its impact on

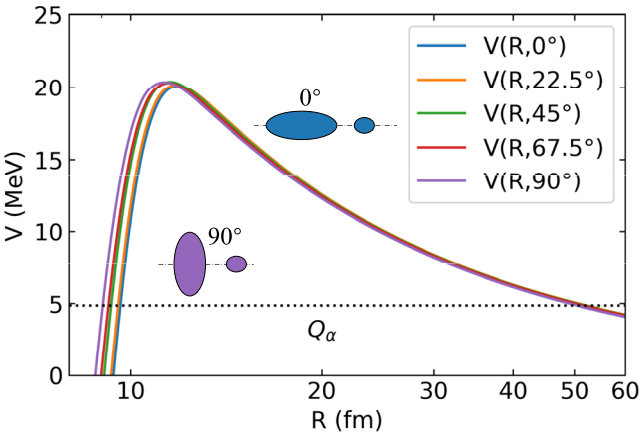

Fig. 2 (Color online) Frozen Hartree–Fock potential for the $\alpha + ^{222}$Rn system with different orientations of ^{222}Rn. In particular, 0° and 90° represent tip and side orientation, respectively. Q_α is the experimental α -decay energy

the nuclear portion remains negligible. This is not surprising, because the intense laser field of intensity 10^{32} W/cm^2 (10^{29} W/cm^2) is comparable to the Coulomb field strength from the daughter nucleus ^{222}Rn at a distance of approximately 66 fm (371 fm). The Coulomb component is defeated by the nuclear component within the core. Therefore, the laser field alters the tunneling points by deforming the long-range Coulomb part of the potential and changing the energy of the emitted particles, thereby affecting the penetration probability.

As shown in Fig. 3, the modification by the laser field becomes observable only when the intensity reaches 10^{32} W/cm^2. Given the current laser technology, no significant modifications in the half-lives were observed experimentally. Nevertheless, even subtle alterations in the potential or decay energy may give rise to discernible effects on the decay processes because tunneling is highly sensitive to the internuclear potential. This is illustrated in Fig. 4. The relative change in the penetration probability ΔP can reach 10^{-3} within the accessible laser intensity. In Fig. 4, ΔP is obtained at the moment of the peak electric field strength with a fixed angle $\theta = 0°$. ΔP and the laser intensity I are plotted on a logarithmic scale. As depicted in Fig. 4, the lower the decay energy a parent nucleus has, the greater the relative change in its penetration possibility across different nuclei. Evidently, the parent nucleus ^{144}Nd is susceptible to laser-induced modification. This stems from its relatively low α decay energy, which results in an extended tunneling path, thereby allowing the laser field to exert a prolonged influence on the decay process. At an intensity of 10^{24} W/cm^2, the modification of the penetration possibility is on the order of 0.1% for ^{144}Nd, which is in agreement with Ref. [10, 12].

The laser-assisted α decay modifications for the even–even nuclei also show good agreement with the predictions in Ref. [13, 14]. The above calculations were conducted using the same approximations (dipole and quasistatic approximations) for the laser field and various internuclear potentials.

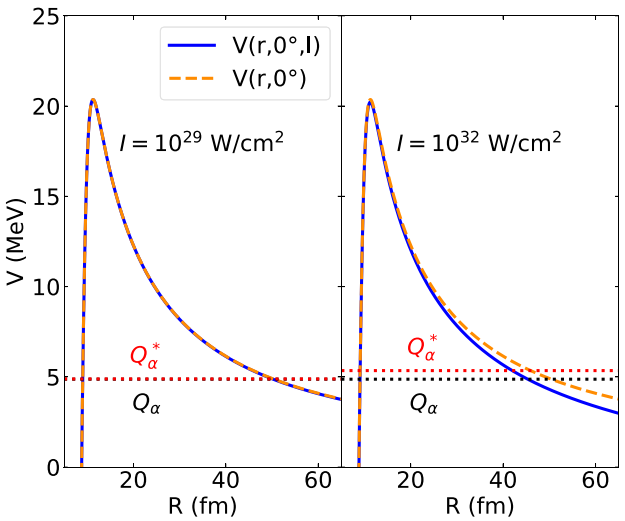

Fig. 3 (Color online) Comparison between laser-free and laser-modified internuclear potentials for the $\alpha + ^{222}$Rn system under two laser intensities, $I = 10^{29}$ W/cm^2 and 10^{32} W/cm^2. 0° represents the tip orientation of ^{222}Rn. The solid line stands for the laser-modified case, and the dashed line stands for the laser-free case. The dotted line represents the α emission energy, where Q_α is the experimental α decay energy, and Q_α^* is the energy of the emitted α particle accelerated by the laser field

Some studies [10, 12–14] employed the phenomenological internuclear potentials, whereas this work utilized the microscopic potentials and considered nuclear deformation effects. Although the results are similar, the FHF method helps pursue a more microscopic understanding of laser-assisted α decay and cluster radioactivity in a self-consistent manner. In addition, in contrast to the modest impact of the laser field predicted by our model, several studies [15–19] have suggested a significant alteration in the alpha decay processes under current laser intensities. These calculations were obtained by solving the time-dependent Schrödinger

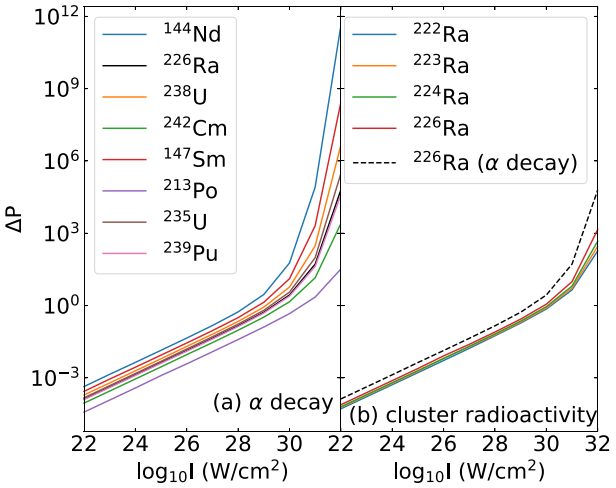

Fig. 4 (Color online) Relative change in penetration possibility $\Delta P(t_0, \theta_0, I)$ for **a** α decay and **b** ^{14}C cluster radioactivity at the moment t_0 of the peak electric field strength with a fixed angle $\theta_0 = 0°$. The dashed line in **b** represents ΔP for α decay of parent nucleus ^{226}Ra

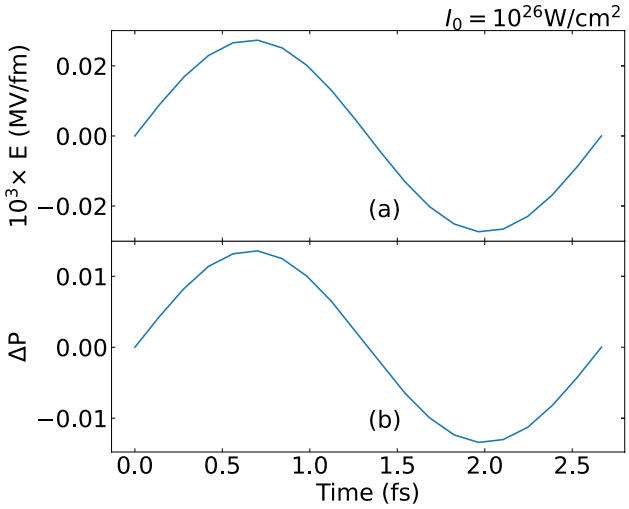

Fig. 5 (Color online) **a** Linearly polarized laser electric field strength E and (b) relative modification of penetration possibility $\Delta P(t, \theta_0, I_0)$ at a fixed angle $\theta_0 = 0°$ as a function of time. The intensity I_0 is 10^{26} W/cm^2 for the $\alpha + ^{222}$ Rn system

equation within the oscillating Kramers–Henneberger frame. The critical assumption was the continuity of the laser field, whereas this study was based on the premise of a single laser pulse. This discrepancy in laser conditions resulted in substantial differences in the respective predictions. However, high-intensity continuous laser fields are unattainable. The potential for future technological advancements in continuous laser technology presents an intriguing area for exploration with the promise of inducing more pronounced modifications in α decay processes.

A comparison of ΔP between α decay and cluster radioactivity for the same parent nucleus, ^{226}Ra, was made. As shown in Fig. 4b, ΔP for α decay is larger than that for cluster radioactivity of any parent nucleus shown here. This can be illustrated by the sensitivity of tunneling to changes in potential and decay energy. It is known that the α (^{14}C cluster) decay energies used here are approximately 5 MeV (30 MeV) and that the tunneling exit points for α (^{14}C cluster) are approximately 60 fm (25 fm). This implies that the modifications of the laser field in the potential and decay energy for α decay have a larger impact on the decay processes and, subsequently, a higher relative change in the penetration possibility. In addition, ΔP exhibits linear dependence on the laser intensity, whereas the values of the slope change dramatically after 10^{30} W/cm^2. This can be explained using Eq. (22) and Eq. (23) or Eq. (24). At relatively low intensities, ΔP is proportional to $\sqrt{I}$. Only for high intensities, the term $\gamma^{(2)}$ proportional to I is not negligible, leading to an inflection in the curves. It should be noted that the slope of ΔP versus intensity curve is steeper for the alpha decay at extreme intensities. This indicates a higher sensitivity of alpha decay to high laser intensities. Given the increased sensitivity, it is reasonable to extrapolate that the effect of laser acceleration on proton emission should be even more pronounced. Consequently, it is recommended that laser-accelerated proton emission be used as a diagnostic tool for assessing the impact of an intense laser field.

The aforementioned theoretical calculations were implemented at the peak laser electric field strength and a fixed angle $\theta = 0°$. Figure 5 shows the linearly polarized laser electric field strength E and the relative modification of the penetration possibility ΔP at a fixed angle $\theta = 0°$ as a function of time. It is clear that time-dependent E_t and ΔP share a similar variation trend, which can be explained by Eq. (22) and Eq. (23). Theoretically, the laser promotion and suppression effects on the possibility of penetration can be observed throughout a laser pulse circle. However, the best time resolution of the experimental detector is of the order of nanoseconds, which is much larger than the current laser period (of the order of femtoseconds). This implies that we cannot observe a time-dependent alteration in ΔP, as shown in Fig. 5b, but a time averaging result in practice. Therefore, it is necessary to consider the effect of the complete laser period on ΔP.

Figure 6a shows the correlation between ΔP and θ for a circular pulse. As illustrated in Eq. (23), ΔP exhibits a linear correlation with cosθ at some moment t. This explains the large variations in ΔP around 0° and 180° and the lack of modification along 90°. Along one fixed angle, ΔP appears quite symmetric to be canceled by integrating over time. Thus, no net gain would remain for modification. Figure 6b

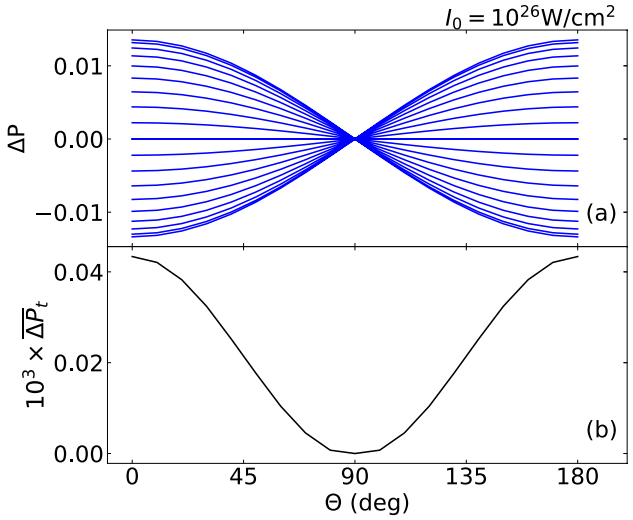

Fig. 6 (Color online) **a** Relative changes in penetration possibility $\Delta P(t, \theta, I_0)$ as a function of angle θ seen from one pulse circle. Various curves depict the scenario at a specific moment t within the pulse cycle. **b** Time-integrated modification $\overline{\Delta P}_t(\theta, I_0)$ as a function of angle θ. θ represents the angle between the directions of the laser field and particle emission. Linear polarization is used here for system α +^{222} Rn at the intensity of $I_0 = 10^{26}$ W/cm^2

shows the time-integrated modification $\overline{\Delta P}_t$ as a function of angle θ. We can infer that some small asymmetries do exist such that a residual net gain remains. As can be observed in Eq. (23), the first equation, involving $\sin\left(\frac{2\pi c}{\lambda}t\right)$, cancels out over time, whereas the second equation remains positive throughout the laser period, contributing to the net gain. The time-integrated modifications are the strongest along 0° and 180°, which are three orders of magnitude smaller than those before integration.

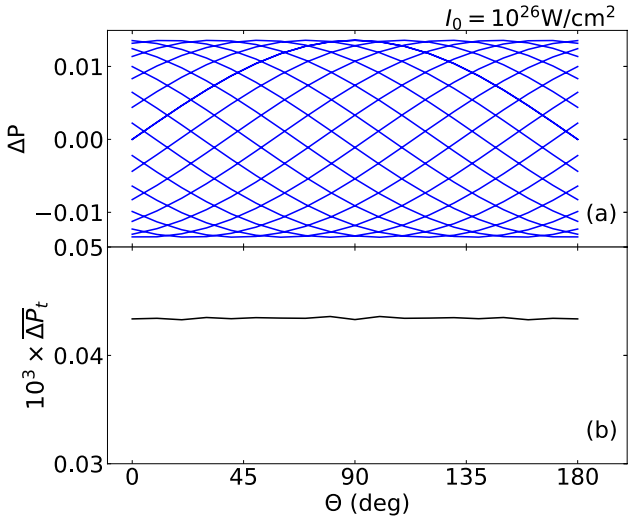

Fig. 7 (Color online) The same as Fig. 6 but for circular polarization

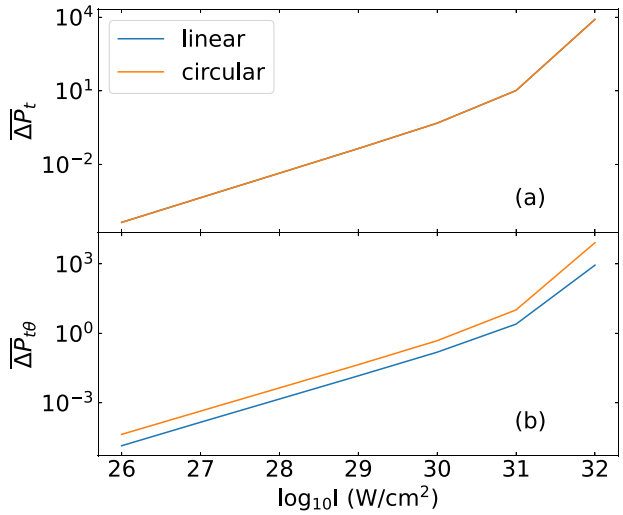

Fig. 8 (Color online) **a** Time-integrated modification $\overline{\Delta P}_t(\theta = 0°, I)$ and **b** time- and angle-integrated modification $\overline{\Delta P}_{t\theta}(I)$ using two polarization methods. The system is α +^{222} Rn

Some studies [59, 60] have explored the potential of elliptically polarized lasers to harness more information from strong-field atomic physics. Circular polarization, a specific manifestation of elliptical polarization, was considered. Figure 7a shows the correlation between ΔP and θ for a pulse circle with circular polarization. Unlike in the linearly polarized case, ΔP in the circular polarization arises from the superposition of $\sin\theta$ and $\cos\theta$, leading to uniformly distributed modifications across all angles. The time-integrated results are presented in Fig. 7b. It can be observed that the time-integrated modification $\overline{\Delta P}_t$ is not affected by the angle between the directions of the laser field and particle emission, emphasizing the advantage of circular polarization in rendering the modification of the penetration possibility free from time averaging. This view coincides with that proposed by Qi et al. [10] who recommended using an elliptically polarized laser over a linearly polarized laser.

As shown in Fig. 6, the linearly polarized laser results in angular anisotropy, with the most significant modifications along 0° and 180°. A comparison of the time-integrated modification $\overline{\Delta P}_t$ along 0° between linear and circular polarizations is shown in Fig. 8a. Both exhibit consistent behavior. In other words, the time-integrated modification $\overline{\Delta P}_t$ in circular polarization maintains the maximum value observed in linear polarization throughout the entire range of angles. This indicates that the primary distinction between the modifications induced by these two types of polarized lasers is associated with their angular distribution characteristics. Xiao et al. [14] indicated that it is important to consider

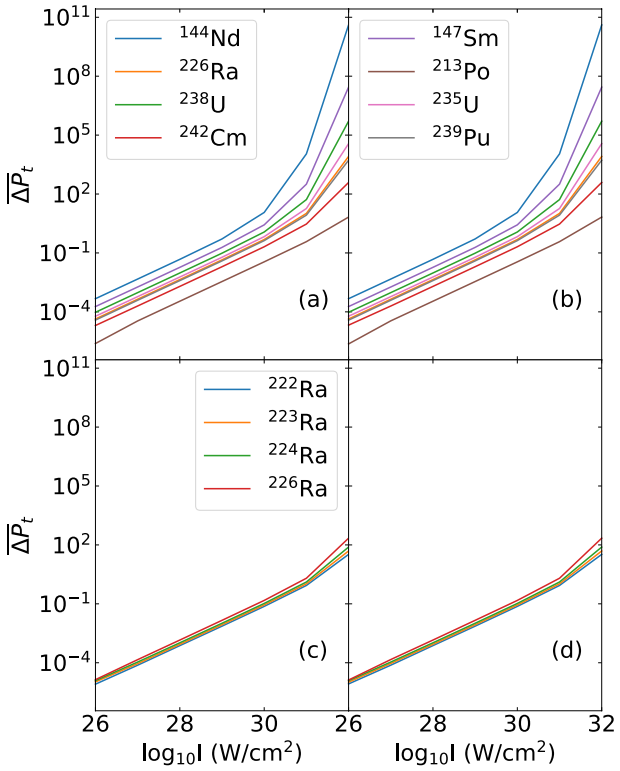

Fig. 9 (Color online) Time-integrated modification $\overline{\Delta P_t}(\theta = 0°, I)$ for **a**, **c** α decay and **b**, **d** ^{14}C cluster radioactivity. The left and right panels refer to the linear and circular polarization, respectively

angular integration because nuclei often appear as a population. The time- and angle-integrated modification $\overline{\Delta P_{t\theta}}$ is represented in Fig. 8b. Evidently, the modification of the circular polarization was several times larger than that of the linear polarization at the same intensity. It is preferable to employ a circularly polarized laser for a more significant modification.

Figure 9 displays the time-integrated modification $\overline{\Delta P_t}$ along 0° for (a) and (c) α decay and (b) and (d) ^{14}C cluster radioactivity across different nuclei. The left and right panels refer to the linear and circular polarizations, respectively. Similar to Fig. 8a, the two polarizations show the same behavior when the angle θ is fixed at 0°. Among these nuclei, ^{144}Nd remains the parent nucleus that is the most susceptible to laser-induced modification, which is attributed to its relatively low decay energy. This modification attained a value of 0.1% at an intensity of 10^{27} W/cm^2, which significantly exceeded the current laser intensity of 10^{28} W/cm^2. A higher intensity of 10^{28} W/cm^2 was required for ^{14}C cluster radioactivity. Notably, additional physical effects are expected when the intensity approaches or surpasses the Schwinger critical field strength [61], whose corresponding laser intensity is

Table 2 Laser intensity I for α decay and cluster radioactivity when the time- and angle-integrated modification $\overline{\Delta P_{t\theta}}$ reaches the order of magnitude of 10^{-3}

Decay channel	$\log_{10}I$	$\overline{\Delta P_{t\theta}}$
^{144}Nd $\rightarrow^{140}$ Ce+α	27	4.66×10^{-3}
^{226}Ra $\rightarrow^{222}$ Rn+α	28	4.39×10^{-3}
^{238}U $\rightarrow^{234}$ Th+α	28	9.51×10^{-3}
^{242}Cm $\rightarrow^{238}$ Pu+α	28	1.97×10^{-3}
^{147}Sm $\rightarrow^{143}$ Nd+α	27	1.84×10^{-3}
^{213}Po $\rightarrow^{209}$ Pb+α	29	3.48×10^{-3}
^{235}U $\rightarrow^{231}$ Th+α	28	5.92×10^{-3}
^{239}Pu $\rightarrow^{235}$ U+α	28	3.89×10^{-3}
^{222}Ra $\rightarrow^{208}$ Pb+^{14}C	29	7.28×10^{-3}
^{223}Ra $\rightarrow^{209}$ Pb+^{14}C	29	8.58×10^{-3}
^{224}Ra $\rightarrow^{210}$ Pb+^{14}C	28	1.03×10^{-3}
^{226}Ra $\rightarrow^{212}$ Pb+^{14}C	28	1.43×10^{-3}

Circular polarization is employed here

2.3×10^{29} W/cm^2. The laser intensity I for circular polarization, where the time- and angle-integrated modification $\overline{\Delta P_{t\theta}}$ reached an order of magnitude of 10^{-3}, is detailed in Table 2. These results are consistent with the scenario where $\theta = 0°$. The modifications reached the order of 0.1% at an intensity of 10^{27} W/cm^2 for α decay and 10^{28} W/cm^2 for cluster radioactivity. Consequently, it is evident that laser-assisted α decay and ^{14}C cluster radioactivity are not practically achievable with current technology.

4 Conclusion

In this study, we conducted a comprehensive microscopic analysis of the effects of extreme laser fields on α decay and cluster radioactivity. Our primary objective was to quantitatively assess the influence of intense laser fields, accounting for their temporal and angular effects, as well as variations in spatial structure. The theoretical framework is based on the Gamow model of quantum mechanical tunneling, whereas the FHF method provides a self-consistent description of the internuclear potential and nuclear deformation effects. The laser–nucleus interaction is represented by an electric field under the dipole approximation.

Our findings indicated that the laser field induced a downward shift in the Coulomb component of the potential and an increase in the decay energy. Given the high sensitivity of quantum tunneling to internuclear potential changes, even minor alterations in the potential or decay energy significantly affect the penetration probability. At an intensity of 10^{24} W/cm^2, the modification in the penetration probability

for the relevant nuclei reached approximately 0.1%, which is consistent with the results reported in Ref. [10].

The time- and angle-dependent modifications of penetration probability were analyzed using both linearly and circularly polarized lasers. In the case of linearly polarized lasers, the penetration probability exhibited its maximum modification at angles of 0° and 180°, with no modification at 90°. Conversely, circularly polarized lasers produced uniformly distributed modifications across all angles, and the angle-integrated modification induced by circular polarization was several times greater than that produced by linear polarization at the same intensity. Nevertheless, the modifications decreased by three orders of magnitude after temporal and angular integrations.

Finally, we compared the time- and angle-integrated modification of the penetration probability induced by circularly polarized lasers for both α decay and ^{14}C cluster radioactivity across various nuclei. Among the studied nuclei, ^{144}Nd was the most susceptible to laser-induced modifications, primarily because of its relatively low decay energy. At an intensity of 10^{27} W/cm^2, the modification of $\overline{\Delta P}_{t\theta}$ for ^{144}Nd reached approximately 0.1%. However, this intensity far exceeds the currently achievable laser intensity of 10^{23} W/cm^2, and the 0.1% modification remains below the detection threshold of the current measurement precision. The effect on the ^{14}C cluster is weaker.

In conclusion, achieving observable laser-assisted α decay and ^{14}C cluster radioactivity requires future advancements in laser technology to significantly enhance the intensity and experimental resolution. Consequently, expectations regarding the feasibility of laser-induced mechanisms for recycling nuclear radioactive waste should be carefully calibrated considering these technological constraints.

Author contributions All authors contributed to the study conception and design. Material preparation, data collection and analysis were performed by Hui Wang, Ying-Ge Huang and Jun Su. The first draft of the manuscript was written by Hui Wang, and all authors commented on previous versions of the manuscript. All authors read and approved the final manuscript.

Data availability The data that support the findings of this study are openly available in Science Data Bank at https://cstr.cn/31253.11.sciencedb.25419 and https://www.doi.org/10.57760/sciencedb.25419.

Declarations

Conflict of interest The authors declare that they have no conflict of interest.

References

1. T. Brabec, H. Kapteyn, *Strong field laser physics*, vol. 1 (Springer, New York, 2008). https://doi.org/10.1007/978-0-387-34755-4
2. M.A. Marques, E.K. Gross, Time-dependent density functional theory. Annu. Rev. Phys. Chem. **55**, 427–455 (2004). https://doi.org/10.1007/b11767107
3. H. Schwoerer, J. Magill, B. Beleites, *Lasers and nuclei: applications of ultrahigh intensity lasers in nuclear science*, vol. 694 (Springer Science & Business Media, 2006). https://doi.org/10.1007/b11559214
4. W. Li, Z. Gan, L. Yu et al., 339 J high-energy Ti: sapphire chirped-pulse amplifier for 10 PW laser facility. Opt. Lett. **43**, 5681–5684 (2018). https://doi.org/10.1364/OL.43.005681
5. L. Yu, Y. Xu, Y. Liu et al., High-contrast front end based on cascaded XPWG and femtosecond OPA for 10-PW-level Ti: sapphire laser. Opt. Express **26**, 2625–2633 (2018). https://doi.org/10.1364/OE.26.002625
6. Ş Mişicu, M. Rizea, Laser-assisted proton radioactivity of spherical and deformed nuclei. J. Phys. G Nucl. Part. Phys. **46**, 115106 (2019). https://doi.org/10.1088/1361-6471/ab1d7c
7. K. Tanaka, K. Spohr, D. Balabanski et al., Current status and highlights of the ELI-NP research program. Matter Radiat. Extremes **5**, 024402 (2020). https://doi.org/10.1063/1.5093535
8. A. Bashinov, A. Gonoskov, A. Kim et al., New horizons for extreme light physics with mega-science project XCELS. Eur. Phys. J. Special Topics **223**, 1105–1112 (2014). https://doi.org/10.1140/epjst/e2014-02161-7
9. H.M. Castañeda Cortés, C. Müller, C.H. Keitel et al., Nuclear recollisions in laser-assisted α decay. Phys. Lett. B **723**, 401–405 (2013). https://doi.org/10.1016/j.physletb.2013.05.025
10. J. Qi, T. Li, R. Xu et al., α decay in intense laser fields: calculations using realistic nuclear potentials. Phys. Rev. C **99**, 044610 (2019). https://doi.org/10.1103/PhysRevC.99.044610
11. A. Pálffy, S.V. Popruzhenko, Can extreme electromagnetic fields accelerate the α decay of nuclei? Phys. Rev. Lett. **124**, 212505 (2020). https://doi.org/10.1103/PhysRevLett.124.212505
12. J. Qi, L. Fu, X. Wang, Nuclear fission in intense laser fields. Phys. Rev. C **102**, 064629 (2020). https://doi.org/10.1103/PhysRevC.102.064629
13. J.H. Cheng, W.Y. Zhang, Q. Xiao et al., Determinants in laser-assisted deformed α decay. Phys. Lett. B **848**, 138322 (2024). https://doi.org/10.1016/j.physletb.2023.138322
14. Q. Xiao, J.H. Cheng, Y.Y. Xu et al., α decay in extreme laser fields within a deformed Gamow-like model. Nucl. Sci. Tech. **35**, 27 (2024). https://doi.org/10.1007/s41365-024-01371-y
15. Ş Mişicu, M. Rizea, α-decay in ultra-intense laser fields. J. Phys. G: Nucl. Part. Phys. **40**, 095101 (2013). https://doi.org/10.1088/0954-3899/40/9/095101
16. D.S. Delion, S.A. Ghinescu, Geiger-nuttall law for nuclei in strong electromagnetic fields. Phys. Rev. Lett. **119**, 202501 (2017). https://doi.org/10.1103/PhysRevLett.119.202501
17. D.P. Kis, R. Szilvasi, Three dimensional α-tunneling in intense laser fields. J. Phys. G: Nucl. Part. Phys. **45**, 045103 (2018). https://doi.org/10.1088/1361-6471/aab0d5
18. D. Bai, D. Deng, Z. Ren, Charged particle emissions in high-frequency alternative electric fields. Nucl. Phys. A **976**, 23–32 (2018). https://doi.org/10.1016/j.nuclphysa.2018.05.004
19. S.A. Ghinescu, D.S. Delion, Coupled-channels analysis of the α decay in strong electromagnetic fields. Phys. Rev. C **101**, 044304 (2020). https://doi.org/10.1103/PhysRevC.101.044304
20. J.H. Cheng, Y. Li, T.P. Yu, Systematic study of laser-assisted proton radioactivity from deformed nuclei. Phys. Rev. C **105**, 024312 (2022). https://doi.org/10.1103/PhysRevC.105.024312
21. F. Queisser, R. Schützhold, Dynamically assisted nuclear fusion. Phys. Rev. C **100**, 041601 (2019). https://doi.org/10.1103/PhysRevC.100.041601
22. W. Lv, H. Duan, J. Liu, Enhanced deuterium-tritium fusion cross sections in the presence of strong electromagnetic fields. Phys.

Rev. C **100**, 064610 (2019). https://doi.org/10.1103/PhysRevC.100.064610
23. S. Liu, H. Duan, D. Ye et al., Deuterium-tritium fusion process in strong laser fields: semiclassical simulation. Phys. Rev. C **104**, 044614 (2021). https://doi.org/10.1103/PhysRevC.104.044614
24. A. Pálffy, H.A. Weidenmüller, Laser-nucleus reactions: Population of states far above yrast and far from stability. Phys. Rev. Lett. **112**, 192502 (2014). https://doi.org/10.1103/PhysRevLett.112.192502
25. L. von der Wense, B. Seiferle, S. Stellmer et al., A laser excitation scheme for ^{229m}Th. Phys. Rev. Lett. **119**, 132503 (2017). https://doi.org/10.1103/PhysRevLett.119.132503
26. W. Wang, J. Zhou, B. Liu et al., Exciting the isomeric ^{229}Th nuclear state via laser-driven electron recollision. Phys. Rev. Lett. **127**, 052501 (2021). https://doi.org/10.1103/PhysRevLett.127.052501
27. A.N. Andreyev, M. Huyse, P. Van Duppen et al., Signatures of the z=82 shell closure in α-decay process. Phys. Rev. Lett. **110**, 242502 (2013). https://doi.org/10.1103/PhysRevLett.110.242502
28. Y.T. Oganessian, F.S. Abdullin, P.D. Bailey et al., Synthesis of a new element with atomic number $z = 117$. Phys. Rev. Lett. **104**, 142502 (2010). https://doi.org/10.1103/PhysRevLett.104.142502
29. A. Sobiczewski, K. Pomorski, Description of structure and properties of superheavy nuclei. Prog. Part. Nucl. Phys. **58**, 292–349 (2007). https://doi.org/10.1016/j.ppnp.2006.05.001
30. T. Otsuka, T. Abe, T. Yoshida et al., α-clustering in atomic nuclei from first principles with statistical learning and the Hoyle state character. Nat. Commun. **13**, 2234 (2022). https://doi.org/10.1038/s41467-022-29582-0
31. J.P. Ebran, E. Khan, T. Nikšić et al., How atomic nuclei cluster. Nature **487**, 341–344 (2012). https://doi.org/10.1038/nature11246
32. J. Magill, J. Galy, T. Žagar, Laser transmutation of nuclear materials, in *Lasers and Nuclei: Applications of Ultrahigh Intensity Lasers in Nuclear Science*. (Springer, Cham, 2006), pp.131–146. https://doi.org/10.1007/3-540-30272-7_9
33. J. Magill, J. Galy, *Radioactivity, radionuclides, radiation*, vol. 259 (Springer, 2005). https://doi.org/10.1007/b138236
34. G. Gamow, Zur quantentheorie des atomkernes. Z. Phys. **51**, 204–212 (1928). https://doi.org/10.1007/BF01343196
35. C. Simenel, Nuclear quantum many-body dynamics: from collective vibrations to heavy-ion collisions. Eur. Phys. J. A **48**, 152 (2012). https://doi.org/10.1140/epja/i2012-12152-0
36. V.Y. Denisov, W. Nörenberg, Entrance channel potentials in the synthesis of the heaviest nuclei. Eur. Phys. J. A-Hadrons Nuclei **15**, 375–388 (2002). https://doi.org/10.1140/epja/i2002-10039-3
37. K. Washiyama, D. Lacroix, Energy dependence of the nucleus-nucleus potential close to the coulomb barrier. Phys. Rev. C **78**, 024610 (2008). https://doi.org/10.1103/PhysRevC.78.024610
38. X.X. Sun, L. Guo, Microscopic study of fusion reactions with a weakly bound nucleus: effects of deformed halo. Phys. Rev. C **107**, L011601 (2023). https://doi.org/10.1103/PhysRevC.107.L011601
39. X.X. Sun, L. Guo, Microscopic study of the hot-fusion reaction ^{48} Ca+^{238} U with the constraints from time-dependent Hartree–Fock theory. Phys. Rev. C **107**, 064609 (2023)
40. C. Simenel, A.S. Umar, K. Godbey et al., How the Pauli exclusion principle affects fusion of atomic nuclei. Phys. Rev. C **95**, 031601 (2017). https://doi.org/10.1103/PhysRevC.95.031601
41. H. Rose, G. Jones, A new kind of natural radioactivity. Nature **307**, 245–247 (1984). https://doi.org/10.1038/307245a0
42. R. Kumar, Cluster radioactivity using various versions of nuclear proximity potentials. Phys. Rev. C **86**, 044612 (2012). https://doi.org/10.1103/PhysRevC.86.044612
43. R. Kumar, M.K. Sharma, Systematic study of various proximity potentials in ^{208}Pb-daughter cluster radioactivity. Phys. Rev. C **85**, 054612 (2012). https://doi.org/10.1103/PhysRevC.85.054612
44. Z. Ren, C. Xu, Z. Wang, New perspective on complex cluster radioactivity of heavy nuclei. Phys. Rev. C **70**, 034304 (2004). https://doi.org/10.1103/PhysRevC.70.034304
45. Y. Qian, Z. Ren, Unified description of α-decay and cluster radioactivity in the trans-tin region. J. Phys. G Nucl. Part. Phys. **39**, 015103 (2011). https://doi.org/10.1088/0954-3899/39/1/015103
46. D. Ni, Z. Ren, T. Dong et al., Unified formula of half-lives for α decay and cluster radioactivity. Phys. Rev. C **78**, 044310 (2008). https://doi.org/10.1103/PhysRevC.78.044310
47. G. Röpke, P. Schuck, Y. Funaki et al., Nuclear clusters bound to doubly magic nuclei: the case of ^{212}Po. Phys. Rev. C **90**, 034304 (2014). https://doi.org/10.1103/PhysRevC.90.034304
48. S. Yang, R. Li, C. Xu, α clustering in nuclei and its impact on the nuclear symmetry energy. Phys. Rev. C **108**, L021303 (2023). https://doi.org/10.1103/PhysRevC.108.L021303
49. C. Xu, Z. Ren, Favored α-decays of medium mass nuclei in density-dependent cluster model. Nucl. Phys. A **760**, 303–316 (2005). https://doi.org/10.1016/j.nuclphysa.2005.06.011
50. C. Xu, Z. Ren, New deformed model of α-decay half-lives with a microscopic potential. Phys. Rev. C **73**, 041301 (2006). https://doi.org/10.1103/PhysRevC.73.041301
51. C. Xu, Z. Ren, Global calculation of α-decay half-lives with a deformed density-dependent cluster model. Phys. Rev. C **74**, 014304 (2006). https://doi.org/10.1103/PhysRevC.74.014304
52. D. Ni, Z. Ren, Half-lives and cluster preformation factors for various cluster emissions in trans-lead nuclei. Phys. Rev. C **82**, 024311 (2010). https://doi.org/10.1103/PhysRevC.82.024311
53. L.J. Qi, D.M. Zhang, S. Luo et al., Cluster radioactivity preformation probability of trans-lead nuclei in the N_pN_n scheme. Phys. Rev. C **108**, 014325 (2023). https://doi.org/10.1103/PhysRevC.108.014325
54. J. Maruhn, P.G. Reinhard, P. Stevenson et al., The TDHF code Sky3D. Comput. Phys. Commun. **185**, 2195–2216 (2014). https://doi.org/10.1016/j.cpc.2014.04.008
55. B. Schuetrumpf, P.G. Reinhard, P. Stevenson et al., The TDHF code Sky3D version 1.1. Comput. Phys. Commun. **229**, 211–213 (2018). https://doi.org/10.1016/j.cpc.2018.03.012
56. P. Stevenson, Y. Shi, E. Yüksel et al., The TDHF code Sky3D version 1.2. Comput. Phys. Commun. **301**, 109239 (2024). https://doi.org/10.1016/j.cpc.2024.109239
57. C. Simenel, A. Umar, Heavy-ion collisions and fission dynamics with the time-dependent Hartree–Fock theory and its extensions. Prog. Part. Nucl. Phys. **103**, 19–66 (2018). https://doi.org/10.1016/j.ppnp.2018.07.002
58. E. Chabanat, P. Bonche, P. Haensel et al., A skyrme parametrization from subnuclear to neutron star densities Part II. nuclei far from stabilities. Nucl. Phys. A **635**, 231–256 (1998). https://doi.org/10.1016/S0375-9474(98)00180-8
59. P. Eckle, A.N. Pfeiffer, C. Cirelli et al., Attosecond ionization and tunneling delay time measurements in helium. Science **322**, 1525–1529 (2008). https://doi.org/10.1126/science.1163439
60. X. Wang, J. Tian, J.H. Eberly, Angular correlation in strong-field double ionization under circular polarization. Phys. Rev. Lett. **110**, 073001 (2013). https://doi.org/10.1103/PhysRevLett.110.073001
61. J. Schwinger, On gauge invariance and vacuum polarization. Phys. Rev. **82**, 664–679 (1951). https://doi.org/10.1103/PhysRev.82.664